

Electrostatically Actuated X-Band Mesh Reflector with Bend-Formed Support Structure

Harsh G. Bhundiyā*, John Z. Zhang†, Kaleb D. Overby‡,

Fabien Royer§, Jeffrey H. Lang¶, Zachary C. Cordero||

Massachusetts Institute of Technology, Cambridge, MA, USA

William F. Moulder **, Sungeun K. Jeon ††, Mark J. Silver ‡‡

MIT Lincoln Laboratory, Lexington, MA, USA

Large reflectors in space (>30 m diameter) can enable advances in communications, remote sensing, and astronomy, by enabling antennas with increased gain, resolution, and bandwidth. However, modern deployable reflectors exhibit a decrease in performance as their diameter increases, due to fabrication errors, slewing, and disturbances on orbit, such as thermal distortion, which decrease surface precision. A potential solution to achieve larger apertures with high precision is to combine in-space manufacturing (ISM) with active control. Herein we demonstrate a reflector concept which combines a candidate ISM process called Bend-Forming with electrostatic actuation to achieve closed-loop control of the reflector surface. We design and fabricate a 1-meter diameter prototype of an electrostatically actuated X-band reflector, using a knitted gold-molybdenum mesh as the reflector surface, carbon fiber-reinforced plastic booms as electrodes, and a truss support structure fabricated with Bend-Forming, a deformation process for constructing trusses from wire feedstock. To characterize the performance of this prototype, we measure its radiation patterns at X-band in an RF anechoic chamber. We successfully demonstrate 1) the stabilization of a pull-in instability with closed-loop control, and 2) beam steering of up to 4.2 degrees with asymmetric electrostatic actuation. Our reflector prototype highlights the opportunities of implementing electrostatically-actuated reflector antennas in space.

I. Nomenclature

A	= area, m^2
b	= damping coefficient, Ns/m
C_0	= capacitance, F
d	= gap distance, m
D	= reflector diameter, m

*Graduate Student, Department of Aeronautics and Astronautics, 77 Massachusetts Ave., Cambridge, MA 02139, AIAA Student Member

†Graduate Student, Department of Mechanical Engineering, 77 Massachusetts Ave., Cambridge, MA 02139, AIAA Student Member

‡Graduate Student, Department of Aeronautics and Astronautics, 77 Massachusetts Ave., Cambridge, MA 02139, AIAA Student Member

§Postdoctoral Researcher, Department of Aeronautics and Astronautics, 77 Massachusetts Ave., Cambridge, MA 02139, AIAA Member

¶Vitesse Professor, Department of Electrical Engineering and Computer Science, 77 Massachusetts Ave., Cambridge, MA 02139

||Boeing Assistant Professor, Department of Aeronautics and Astronautics, 77 Massachusetts Ave., Cambridge, MA 02139, AIAA Member

**Technical Staff, RF Technology, 244 Wood St., Lexington, MA 02421

††Technical Staff, Structural and Thermal Engineering, 244 Wood St., Lexington, MA 02421, AIAA Senior Member

‡‡Assistant Group Leader, Mechanical Engineering, 244 Wood St., Lexington, MA 02421, AIAA Associate Fellow

DISTRIBUTION STATEMENT A. Approved for public release. Distribution is unlimited.

This material is based upon work supported by the Department of the Air Force under Air Force Contract No. FA8702-15-D-0001. Any opinions, findings, conclusions or recommendations expressed in this material are those of the author(s) and do not necessarily reflect the views of the Department of the Air Force. Delivered to the U.S. Government with Unlimited Rights, as defined in DFARS Part 252.227-7013 or 7014 (Feb 2014). Notwithstanding any copyright notice, U.S. Government rights in this work are defined by DFARS 252.227-7013 or DFARS 252.227-7014 as detailed above. Use of this work other than as specifically authorized by the U.S. Government may violate any copyrights that exist in this work. © 2022 Massachusetts Institute of Technology.

δ	=	mesh displacement (near center), m
E	=	electric field, V/m
ϕ	=	electric potential, V
ε	=	RMS surface error, m
ϵ_0	=	vacuum permittivity, F/m
η	=	efficiency
f	=	focal length, m
f/D	=	focal length-to-diameter ratio
F_R	=	radial reaction force, N
F_V	=	vertical reaction force, N
G	=	gain, dBi
HPBW	=	half-power (3-dB) bandwidth, °
k	=	spring constant, N/m
L_b	=	bay sidelength, m
L_t	=	triangle sidelength, m
m	=	mass, kg
N_{attach}	=	mesh attachment points
Q	=	charge, C
R	=	resistance, Ω
T	=	mesh tension, N/m
φ	=	azimuth angle, °
V	=	electric potential, V
V_b	=	bias voltage, V
v_c	=	control voltage, V
ω_0	=	natural frequency, rad/s
f_0	=	natural frequency, Hz
ζ	=	damping ratio
τ	=	electromechanical bandwidth ratio
x	=	displacement, m
w	=	membrane displacement, m
P	=	pressure, Pa

II. Introduction

Large space reflectors (>30 m diameter) can enable performance benefits in numerous fields (e.g., communications, remote sensing, astronomy) by achieving higher gain and resolution, reducing the size of ground stations, and enabling novel applications like microwave radiometry from geostationary orbit [1]. Despite these advantages, today the performance of large space reflectors is limited by launch packaging constraints which restrict their aperture size; and fabrication errors and thermal distortions which decrease the precision of the reflector surface [2, 3]. Indeed, modern deployable reflectors exhibit a linear decrease in surface precision as their diameters increase, following a typical surface-error-to-diameter ratio of $\varepsilon/D = 10^{-4}$, as depicted in Figure 1 (adapted from [4]). This observed tradeoff between diameter and surface precision has limited reflector sizes to tens of meters, limiting their use for missions which require both large apertures and high precision, such as in astronomy and surveillance. For large reflectors, an additional challenge is achieving a fast slew rate, which becomes difficult due to the lower damping and lower natural frequency of the supporting structure.

A candidate solution to circumvent launch packaging constraints is via in-space manufacturing (ISM), which refers to robotically fabricating structures on orbit from raw feedstock. This approach offers the unique opportunity for fabrication of structures optimized for the space environment and potentially larger structures than can be achieved with deployable systems today. A wide range of feedstock materials and processing methods have been proposed for ISM, including additive manufacturing of metallic and fiber-reinforced composite feedstocks [5, 6]; extrusion of fiber-reinforced plastics [7]; and deformation processing of metals via plastic deformation [8, 9]. A recent comparison of these processes [10] has found that deformation processing is a promising ISM approach for fabricating large structures on orbit due to its low specific energy consumption. However, one challenge with ISM processes (including deformation processes) is the accuracy of fabricated structures, which is dictated by the error stack-up of individual fabrication steps

and can result in residual stress and imperfect geometries at the end of fabrication. Such defects can negate the benefit of larger structures possible with ISM by decreasing their precision below the required performance metrics.

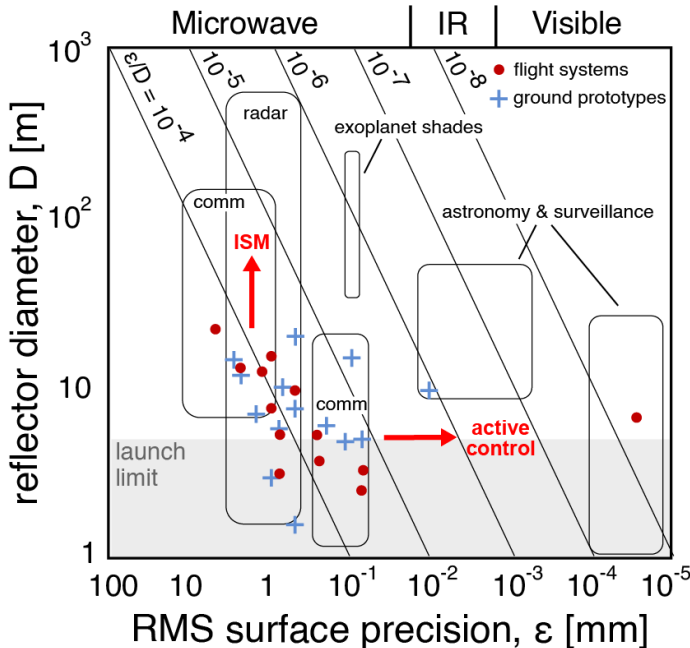


Fig. 1 Diameter and root-means-square (RMS) surface precision of modern deployable space reflectors compared against requirements for specific applications (adapted from [4]). A tradeoff between diameter and surface precision has limited the practical size of reflectors to tens of meters. In-space manufacturing (ISM) and active control via electrostatic actuation may enable larger reflectors with improved precision.

Hence to achieve both large-diameter and precise structures, ISM must be combined with another method of increasing global accuracy, such as active control. For applications such as reflectors, electrostatic actuation is attractive for active control, as it requires low power, adds little structural mass to the spacecraft, and is easily scalable. For instance, by placing electrodes on a command surface a fixed distance away from a conductive reflector surface, an initially flat surface can be pulled into a target parabolic shape by applying a bias voltage between the two surfaces. With multiple electrodes and closed-loop control, the reflector surface can be precisely contoured to maintain the desired shape in the presence of disturbances [11, 12]. In this way electrostatic actuation can enable the *in situ* correction of disturbances, adjustment of focal length, and even beam steering of reflector surfaces.

Originally pioneered in the 1980s [11–13], this concept of an electrostatically-actuated reflector surface has been studied for over 40 years, leading to various ground demonstrations. In 1980, for instance, NASA developed a 4.88-meter diameter polyimide membrane reflector controlled with concentric-ring electrodes, achieving a RMS surface accuracy of 15 μm with voltages below 70 kV [13]. Later in 2006, SRS Technologies successfully retrofitted an AstroMesh deployable antenna with thin film electrodes, demonstrating electrostatic actuation of a 5-meter diameter polyimide membrane [14]. In 2018, Xidian University demonstrated a 2-meter diameter electrostatically-actuated reflector, achieving a surface accuracy of 0.25 mm with triangular electrodes below a polyimide membrane [15, 16]. Despite these demonstrations, large electrostatically-actuated reflectors have not been implemented in space, due to challenges with pull-in instabilities and the complexities of electrostatic actuation in the space environment. For instance, it is unclear how charge accumulation, plasma, and ionizing radiation would affect electrostatic actuation of large surfaces on orbit. Nonetheless, electrostatically-actuated reflectors show promise for large space antennas, given the growing demand for larger apertures in communications, remote sensing, and astronomy.

In this paper, we pursue a ground demonstration of an electrostatically-actuated mesh reflector, combining the unique capabilities of an ISM process called Bend-Forming and active control via electrostatic actuation. Unlike previous ground demonstrations which use a polymer membrane as the reflector surface, we use a knitted gold-molybdenum mesh, a material often used in modern deployable reflectors [17]. Additionally, unlike previous studies, we implement electrostatic actuation with closed-loop control to demonstrate stabilization of pull-in instabilities; and we present

asymmetric electrostatic actuation to achieve beam steering. We demonstrate these capabilities on a physical prototype, which uses carbon fiber-reinforced plastic (CFRP) booms as electrodes and a ring truss as support structure for the reflector. This support structure is fabricated with Bend-Forming, a robotic deformation process which combines CNC wire bending with solid-state joining to form trusses via plastic deformation [9]. This process is uniquely suited to fabrication in space as it has low energy consumption, is amenable to stiff feedstock materials, and is easily automated. Hence by combining the enabling capabilities of closed-loop electrostatic actuation, CFRP electrodes, and the Bend-Forming process, we present our results in the design, fabrication, and characterization of a 1-meter diameter electrostatically-actuated mesh reflector. With our prototype we successfully demonstrate 1) the stabilization of pull-in instabilities with closed-loop control; and 2) beam steering of up to 4.2 degrees with asymmetric electrostatic actuation.

The paper is organized as follows. Section III describes the design, fabrication, and electrostatic actuation of our reflector prototype. Section IV presents its radiation patterns measured at the Compact Range Facility of MIT Lincoln Laboratory [18], which demonstrate closed-loop and asymmetric electrostatic actuation. Finally Section V summarizes the results and provides an outlook which highlights the challenges and opportunities of electrostatically-actuated reflectors in space.

III. Methods: Reflector Demonstration

An image of our electrostatically-actuated reflector prototype is shown in Figure 2. The prototype consists of three main components: a 1-m diameter, knitted gold-molybdenum mesh; truss support structure around the mesh circumference; and a command surface of carbon fiber-reinforced plastic (CFRP) electrodes at a fixed distance from the mesh. The knitted gold-molybdenum mesh has 40 openings per inch (OPI) which is designed for high-frequency operation at X-band (8-12 GHz); the truss support structure is fabricated from 1 mm steel wire with Bend-Forming; and the CFRP electrodes are fabricated with an out-of-autoclave (OOA) molding process. Section III.A and Section III.B further describe the design and fabrication of the truss support structure and CFRP electrodes.

To achieve electrostatic actuation, we apply a bias voltage of up to 30 kV between the mesh and command surface using a high-voltage power supply to deform the mesh towards the electrodes and form a curved shape which serves as the reflector surface. Since the electrostatic force is spring-weakening, an instability (known as “pull-in” [19]) occurs past a certain displacement when operating with open-loop control. To stabilize displacements past this pull-in instability, a ± 5 kHz high bandwidth amplifier is used to adjust the voltage on the command surface and prevent the electrostatic force from increasing monotonically as the mesh draws closer to the command surface. To this end, we measure the deflection of the mesh near its center with a laser displacement sensor (as depicted in Figure 2) and calculate a displacement error based on a look-up table of bias voltage vs displacement for a single-degree-of-freedom (sdof) system. This error is used to control the output of the amplifier with a proportional-integral controller running on a FPGA with a 100 kHz loop rate. To achieve asymmetric electrostatic actuation (i.e., beam steering), we use the amplifier to adjust voltage on only half of the command surface while the other half is grounded. Further details of the electrostatic actuation and control schemes are provided in Section III.C.

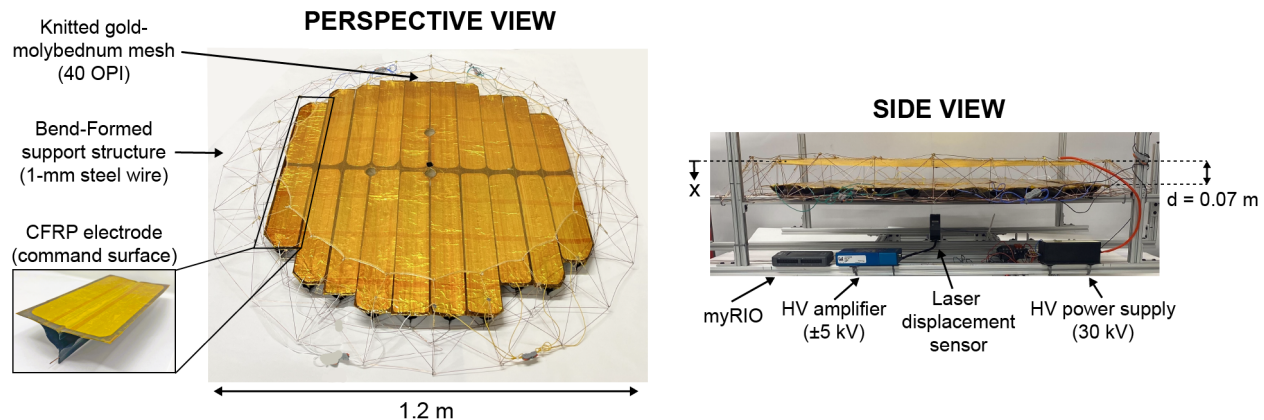


Fig. 2 Prototype of an electrostatically-actuated mesh reflector. A bias voltage of up to 30 kV is applied between the mesh and command surfaces to deform the mesh into a curved shape. A laser displacement sensor measures the mesh deflection (δ) and enables closed-loop actuation via a ± 5 kHz high bandwidth amplifier.

A. Bend-Formed Support Structure

Here we describe the design and fabrication of the Bend-Formed support structure for the prototype shown in Figure 2. The key design requirement for the support structure is to provide radial and vertical reaction forces at the mesh attachment points as the mesh deflects towards the electrodes in response to the applied bias voltage. Modeling the mesh as a thin circular membrane with diameter D and uniform tension T (N/m), the radial reaction force (F_R) at each attachment point is

$$F_R = \frac{\pi D T}{N_{\text{attach}}}, \quad (1)$$

where N_{attach} is the number of attachment points around the mesh circumference. Additionally, modeling the mesh and command surfaces as flat parallel plates separated by a gap distance d (further described in Section III.C), the vertical reaction force (F_V) on the support structure equilibrates with the electrostatic force on the mesh, expressed as

$$F_V = \frac{1}{2} \epsilon_0 \left(\frac{V}{d} \right)^2 \frac{A}{N_{\text{attach}}}, \quad (2)$$

where ϵ_0 is the vacuum permittivity, V is the voltage applied between the mesh and command surface, A is the electrode area, and d is the gap distance. Hence, for a given maximum mesh tension T_{\max} and a maximum bias voltage V_{\max} , the support structure must be designed to not buckle under the maximum radial and vertical forces given by Equation (1) and Equation (2). The support structure must also be designed to provide a sufficient gap distance between the mesh and command surfaces, so that the desired reflector shape can be achieved without collision and electrostatic breakdown between the two surfaces.

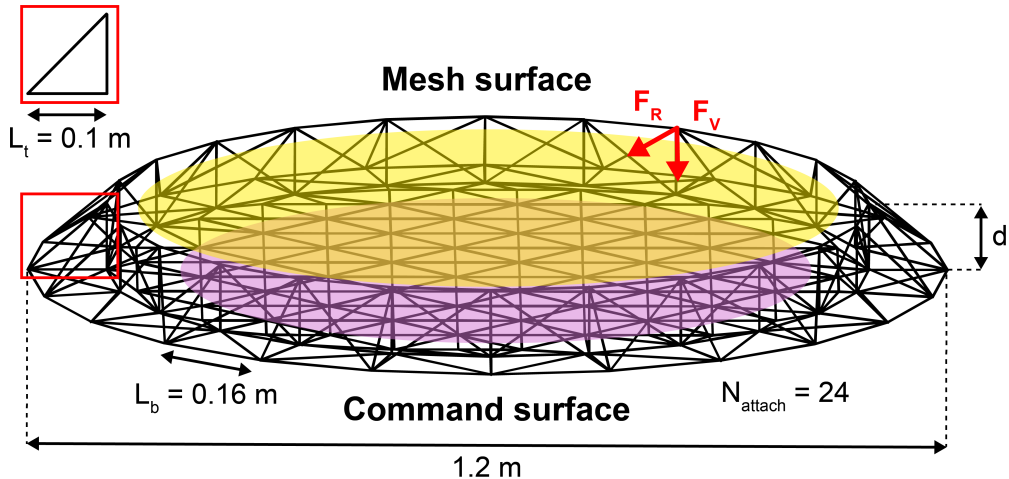


Fig. 3 Truss support structure for the reflector prototype. A ring truss with a right, equilateral triangle cross section supports the mesh (gold) around its circumference, and an inner triangular grid supports the electrodes of the command surface (purple).

Considering these design requirements, we pursue a structural concept consisting of a ring truss which attaches to the mesh around its circumference, and an inner triangular grid which supports the electrodes of the command surface. The ring truss consists of bays with a right, equilateral triangle cross section and alternating diagonals, as depicted in Figure 3. For our prototype, we chose $N_{\text{attach}} = 24$ mesh attachment points, a bay sidelength of $L_b = 0.16$ m, a triangle cross section of $L_t = 0.1$ m, and a gap distance of $d = 0.1$ m. These dimensions were chosen to support a mesh surface with diameter $D = 1$ m, a maximum voltage of $V_{\max} = 30$ kV, and a representative maximum mesh tension. To verify that the radial and vertical buckling loads of the support structure were greater than the corresponding forces given by Equation (1) and Equation (2), a finite element analysis was conducted in *Abaqus*, using beam elements (B31) and a buckling eigenvalue analysis step. Modeling the structure with 1-mm steel wire ($E = 200$ GPa, $\nu = 0.29$) and assuming rigid joints at the nodes, radial and vertical loads were applied to the mesh attachment points with pinned boundary conditions at the bottom nodes of the ring. This analysis resulted in the critical radial and vertical buckling loads $F_R^* = 1.69$ N and $F_V^* = 15.0$ N, which were deemed sufficient to support the radial and vertical forces given by Equation (1) and Equation (2).

To fabricate the structural concept of Figure 3, the deformation process of Bend-Forming was used, which combines CNC wire bending with mechanical joints to construct reticulated structures from wire feedstock [9]. In particular, a bend path was found which continuously traverses all edges of the geometry and converted to fabrication instructions for a CNC wire bender. For the prototype shown in Figure 2, separate bend paths were computed for the ring truss and inner triangular grid and combined to form a single bend path for the full structure. The corresponding fabrication instructions were implemented on the DI Wire Pro, a desktop CNC wire bender [20], with 1-mm diameter steel wire as the feedstock. Finally solder joints were added to the nodes, resulting in the support structure shown in Figure 2. Due to fabrication defects of the Bend-Forming process (e.g. feed length error, angular error, and nonzero strut curvature), the final geometry of the truss support structure was not identical to the perfect geometry of Figure 3 and contained defects such as buckled struts and nonplanar mesh attachment points. However, the mesh was attached to the top nodes of the ring truss via cables, and the electrodes of the command surfaces were attached to the inner triangular grid via wire slots (further described in Section III.B). The attachment of the CFRP electrodes resulted in a final gap distance between the mesh and command surfaces of $d \approx 0.07$ m (see Figure 2). Additionally, a small hole was cut in an electrode near the center of the prototype to allow measurement of the mesh displacement with a laser displacement sensor.

B. Command Surface

Here we describe the design and fabrication of electrodes used as the command surface for the prototype shown in Figure 2. The goal of the command surface is to provide a surface opposite the mesh such that when an electric potential is applied, the electrostatic force deforms the mesh into a curved shape. The Bend-Formed support structure alone does not provide a suitable command surface since 1) it has low out-of-plane stiffness and thus easily deflects in the direction of the electric field; 2) it does not readily permit individually addressable electrodes necessary for controlling asymmetric actuation, as it is made from a single strand of wire; and 3) the electrostatic force generated is less than what is possible with a non-porous surface.

While the first two limitations are obvious based on the structural concept shown in Figure 3, the latter is less so. To understand, Glover et al. [21] begins with the method of images to determine the electric field between a cylindrical conductor and a plate. If we consider a wire of radius r and linear charge density λ at a vertical distance h above a planar ground surface, the electric field on the planar surface a horizontal distance w away from a reference point directly below the wire is given by,

$$E_{\text{ground surface}} = \frac{\lambda}{2\pi\epsilon_0} \frac{2h}{h^2 + w^2} = aV \frac{2h}{h^2 + w^2}, \quad (3)$$

where by using the method of images, we know the capacitance between two cylindrical conductors of radii r_1 and r_2 separated by a distance k is [21]

$$C = \frac{Q}{V} = \frac{\pi\epsilon_0}{\ln \frac{k}{\sqrt{r_1 r_2}}} \quad (4)$$

and therefore $\frac{\lambda}{2\pi\epsilon_0}$ becomes aV with some constant a . For a planar surface we assume parallel plates, thus

$$E_{\text{plate}} = V \frac{1}{k} \quad (5)$$

The spacing between wires in the Bend-Formed structure of grid is on the order of 10 cm. This spacing dictates the variable w , which in our system is the horizontal distance from the wire to a point of interest on the mesh. For a sufficiently small gap d , we can see from Equation (3) that as w increases, the electric field decreases, and hence so does the electrostatic force at that point on the mesh surface. On the other hand, with a planar electrode surface, the electric field of Equation (5) stays constant across the mesh surface. This explains the faceting behavior of the mesh and decreased total force when using a wireframe structure rather than planar electrodes as the command surface.

Given these limitations of a wireframe command surface, we instead implemented a command surface made from carbon fiber reinforced plastic (CFRP) booms as shown in Figure 4. These booms serve two purposes: 1) they increase the global stiffness of the structure and 2) they act as individually addressable, planar electrodes. The booms were designed to have a large planar area while being compatible with Bend-Forming: flattenable and able to attach to the wireframe structure. To maintain consistent, predictable electrostatic pressure, they were optimized to minimize deflection in the y-direction as annotated in Figure 4. By finite element analysis with *Abaqus*, the maximum deflection for an electrostatic pressure up to 100 Pa was 1.605 mm.

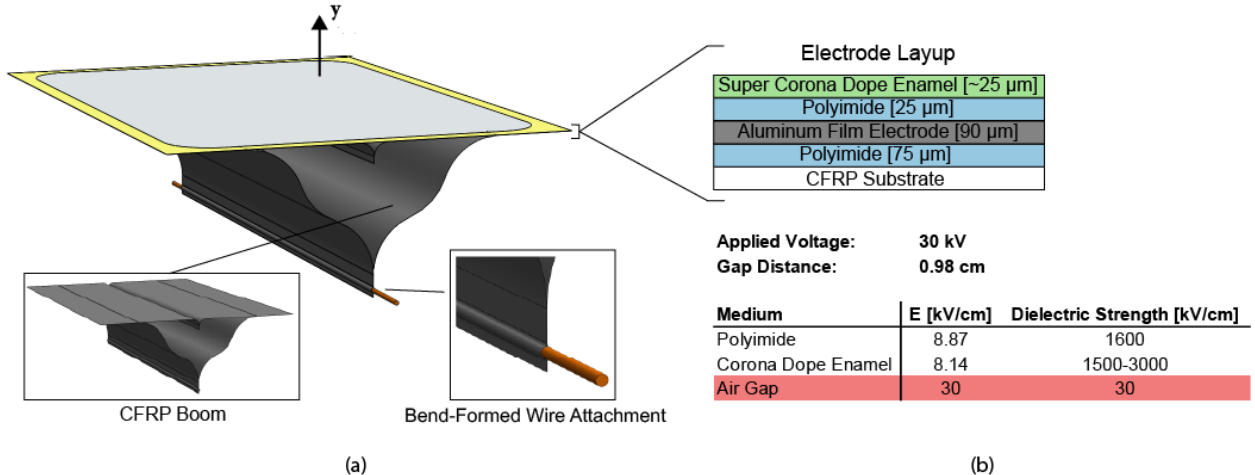


Fig. 4 (a) The command surface electrode is composed of a CFRP boom with an aluminum film electrode and dielectric layup fixed atop. The boom is attached to the Bend-Formed structure via the wire slot. (b) The electric field within each material at breakdown for an applied voltage of 30 kV and a gap distance of 0.98 cm. Breakdown is predicted to occur within the air gap, where the electric field exceeds dielectric strength.

Implementing the unique cross section design was enabled by a silicone molding, out-of-autoclave (OOA) manufacturing method [22, 23]. Silicone molds were created according to the cross section design and CFRP prepreg was layed up within the silicone forms. When inserted into a rigid, metal container and heated to an elevated temperature for curing, the incompressible silicone expands due to thermal expansion. This restricted expansion generates high pressures onto the carbon fiber layers, thereby decreasing void content and approaching the desired cross section form.

To enable the CFRP booms to serve as individually addressable electrodes for our prototype in standard atmospheric conditions, we applied a layup of various conducting and nonconducting materials. This layup insulated the electrode from the CFRP and provided dielectric strength to prevent breakdown over the desired range of voltages. The layup consisted of materials with corresponding thicknesses identified in Figure 4 to prevent breakdown between the aluminum electrode and the mesh as it deflected within our desired range and up to a maximum bias voltage of $(V_b)_{\max} = 30 \text{ kV}$. Additionally, for asymmetric actuation, it was critical to prevent breakdown between adjacent electrodes and structural components up to a maximum control voltage of $(v_c)_{\max} = 10 \text{ kV}$. To determine the suitability of the CFRP electrode, we compared the electric field between the mesh and command surfaces with the dielectric strengths of the various materials within the gap distance. We first ignored the fringing effects at the edges of the electrode and modeled the two surfaces as parallel plates.

For parallel plates, the electric field lines are normal to the electrode surfaces and given by the electric potential (ϕ) so that

$$E = -\frac{\partial \phi}{\partial y}, \quad (6)$$

which since the change in voltage through a single medium is linear, may be written as

$$E_i = -\left(\frac{\phi_j - \phi_{j+1}}{t_i}\right) \quad (7)$$

where i represents the respective medium through which the electric field is determined. The medium is bounded by interfaces j and $j + 1$. For i materials and $i + 1$ interfaces, the system can be solved for E within each material using the interface condition that the normal electric displacement flux is continuous.

Figure 4 (b) indicates the resulting voltage and electric field within each medium between the command surface and the mesh when $V = 30 \text{ kV}$. Breakdown occurs if the electric field present in each material exceeds the respective dielectric strength. For the given material layup and $V = 30 \text{ kV}$, breakdown was estimated at a gap distance of 0.98 cm. The dielectric strength of air at 0°C and 760 Torr is 30 kV/cm, which would indicate a gap distance of 1.0 cm at breakdown [24]. Accordingly, the air gap is dominant and the dielectric layup marginally improved the breakdown strength. Experimentally, breakdown occurred at gap distances of 1.5 cm at $24 \text{ kV} < V < 27 \text{ kV}$. The reason for such differences was likely due fringe effects at the edges of the command surface electrodes.

We found that polyimide and dielectric enamel noticeably improved breakdown prevention at the edges of electrodes, where arcing was visibly identified to occur. If we consider the edges of the electrode to be thin wires of small radii r , we may model the electric field between them and the mesh as well as between two adjacent edges as done in [21]. The maximum electric field occurs at the surface of the wire (i.e. the edge of the rectangular electrode) and is equivalent to

$$E = \frac{\lambda}{2\pi\epsilon r} \quad (8)$$

From Equation (4), and assuming two wires of equal radii, this becomes

$$E = \frac{V}{2r \ln \frac{k}{r}} \quad (9)$$

To estimate the electric field between edges of adjacent electrodes in our system, we set $k = 2 \text{ cm}$, $r = 100 \mu\text{m}$, and $V = 25 \text{ kV}$ which yields an electric field of 236 kV/cm . This high field concentration is greater than the dielectric strength of air alone hence requiring the usage of high strength dielectric layup. Typical dielectric strength of polyimide tape is between $1500\text{-}3000 \text{ kV/cm}$ providing the necessary protection to prevent breakdown.

Therefore, it may be concluded that the dielectric layup marginally improved the breakdown prevention between the mesh and command surface within the planar regions of the booms. However, at the edges, the dielectric layup markedly prevented breakdown due to the high field concentrations within the region.

The electrode pattern presented in this work was not the optimal arrangement for shaping the mesh or stiffening the structure. The design was chosen based on time constraints and ease of manufacturing. As a result, the electrode pattern had 10 degrees of freedom in one direction, while having two in the perpendicular, i.e. the command surface voltage could be spatially varied by 10 increments versus two. Additionally, the parallel organization of CFRP booms created an orthotropic structure, where the bending stiffness along the axis of the booms was much greater than in the transverse direction. Rather than the parallel electrode pattern, a concentric rectangular ring pattern would have improved upon both drawbacks. It would permit equivalent degrees of freedom in the two primary axes while also creating a structure closer to planar quasi-isotropic stiffness. More rigorous approaches to electrode patterning are developed in [25, 26], although maintaining compatibility with Bend-Forming limits the design space.

C. Electrostatic Actuation and Control

Electrostatic actuation of the mesh reflector can be thought of as a continuum electromechanical system. In equilibrium, the electric field between the mesh and the command surface is governed by Laplace's equation for electrostatics and the displacement field is governed by the force balance between the electrostatic spring-weakening force and the restoring force of the mesh stiffness. We elucidate the key physics of this system using a single degree-of-freedom (sdof) model illustrated in Figure 5.

For the sdof model shown in Figure 5, the dynamics of the system are governed by two equations

$$\underbrace{m\ddot{x} + b\dot{x} + kx = \frac{Q^2}{2\epsilon_0 A}}_{\text{mechanical}} \quad \text{and} \quad \underbrace{\dot{Q} = \frac{1}{R} \left(V - \frac{Q(d-x)}{\epsilon_0 A} \right)}_{\text{electrical}}, \quad (10)$$

where m is the mass, b is the damping, k is the spring constant, Q is the charge on the mesh, ϵ_0 is the permittivity of vacuum, A is the electrode area, R is resistance, d is the initial gap, and $V = V_b - v_c$ is the voltage difference across the mesh and the command surface. It is easier to work with the equations in non-dimensional form where we normalize using the gap distance (d), natural frequency of the spring (ω_o), and the charge and voltage at pull-in (q^*, v^*):

$$\hat{x} = \frac{x}{d}, \quad \hat{t} = \omega_0 t, \quad \hat{q} = \frac{Q}{q^*}, \quad \hat{v} = \frac{V}{v^*}. \quad (11)$$

Here $\omega_0 = \sqrt{\frac{k}{m}}$, $q^* = \frac{3}{2} C_0 v^*$, and $v^* = \sqrt{\frac{8kd^2}{27C_0}}$, where $C_0 = \frac{\epsilon_0 A}{d}$ is the initial capacitance of the parallel plate capacitor. For simplicity of notation, we drop the hats in this section for the non-dimensional variables.

We thereby obtain two non-dimensional coupled differential equations which govern the deformation and charging of the mesh surface with time,

$$\ddot{x} + 2\zeta\dot{x} + x = \frac{1}{3}q^2 \quad \text{and} \quad \tau\dot{q} + (1-x)q = \frac{2}{3}v, \quad (12)$$

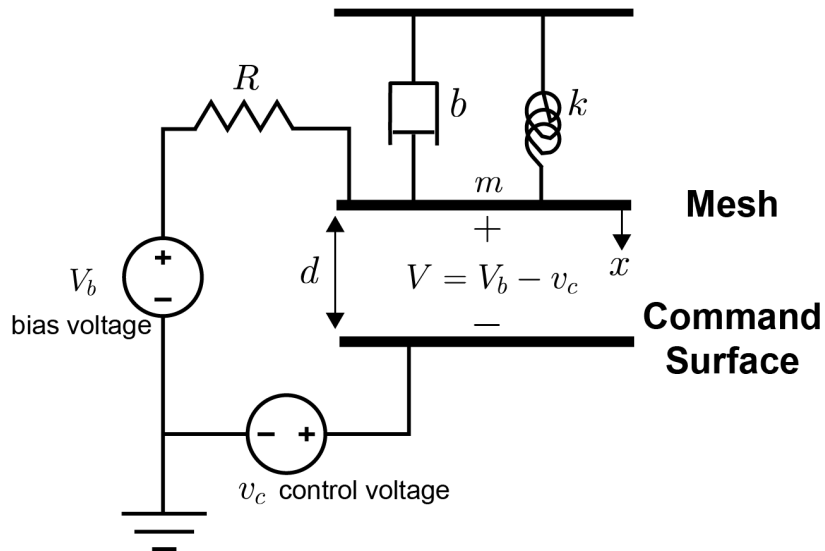


Fig. 5 Single degree-of-freedom electrostatic capacitor actuator.

where $\zeta = \frac{b}{2m\omega_0}$ and $\tau = \omega_0 RC_0$ are related to damping and the ratio of bandwidths for the mechanical and electrical dynamics. If the resistance goes to zero or the capacitance is particularly small then the charge dynamics disappear and we recover the equation

$$m\ddot{x} + b\dot{x} + kx = \frac{1}{2}\epsilon_0 A \frac{1}{(d-x)^2} V^2, \quad (13)$$

which considers only dynamics of the mechanical system with a voltage-controlled nonlinear force. Note for the infinite parallel plate approximation a constant charge gives rise to a constant force since the electric field does not depend on the geometry such as the gap distance. It is advantageous to work with the charge as an additional state since the voltage-driven system is parametric and the addition of charge is useful for analyzing disturbances due to environmental plasma and current limits of the amplifier.

Using the following choices of states, $x_1(t) = x(t)$, $x_2(t) = \dot{x}(t)$, and $x_3(t) = q(t)$, the final non-dimensional state space equations are then

$$\dot{\mathbf{x}}(t) = \begin{pmatrix} \dot{x}_1(t) \\ \dot{x}_2(t) \\ \dot{x}_3(t) \end{pmatrix} = \begin{pmatrix} x_2 \\ -2\zeta x_2 - x_1 + \frac{1}{3}x_3^2 \\ -\frac{1}{\tau}(1-x_1)x_3 + \frac{2}{3r}v \end{pmatrix}. \quad (14)$$

The stationary points X_i relating charge to displacement is satisfied by $X_1 = \frac{1}{3}X_3^2$, which can be re-expressed in terms of voltage with some algebra. The region of this curve below $x < 1/3$ is stable while the region above $x > 1/3$ is unstable.

As indicated in Figure 6, after pull-in, displacement increases with a decreasing potential difference. This counter-intuitive effect is due to the nonlinear nature of the force in relation to the voltage. As the mesh approaches the command surface, the electrostatic force increases at a rate dramatically faster than the restoring elastic force of the mesh. If left to its own devices, this force will seek to further decrease the gap and pull the mesh until it touches the command surface (for our prototype this results in dielectric breakdown before the surfaces come into contact). However, a control loop with sufficient bandwidth is capable of stabilizing this unstable behavior by carefully adjusting the voltage so that the two forces balance even in the event that the growth of the electrostatic force is high in the unstable region. The end result is a controller that is adjusting a constantly varying voltage that happens to be lower than the pull-in voltage needed to initially reach the unstable region.

If the voltage is increased at a sufficiently slow rate or the damping of the system is significant, the sdof model will have a pull-in curve dictated by the expression

$$v = \sqrt{\frac{27}{4}} \sqrt{x}(1-x). \quad (15)$$

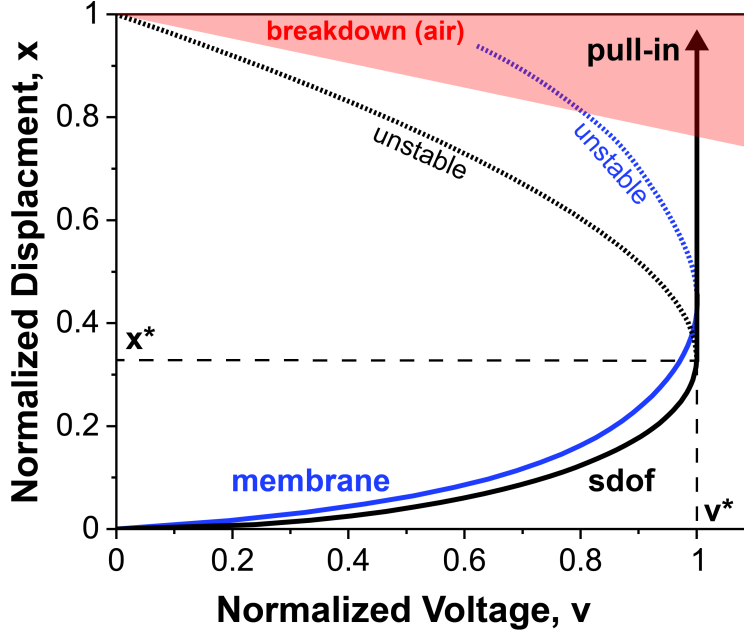


Fig. 6 Normalized pull-in curve for a sdof capacitor actuator. A typical membrane pull-in curve with a deeper inflection point is shown in blue as simulated using COMSOL Multiphysics. The red indicates the region in which breakdown occurs in air (30 kV/cm). This region changes for various altitudes in space.

An inverse function relating voltage to displacement can be obtained, but the expression is unwieldy. For the sdof model, the critical pull-in displacement is always 1/3 of the gap distance.

In continuum systems, such as plates, membranes, or beams, the pull-in point is found to be almost always deeper [19]. A membrane type pull-in curve is computed using full electrostatic and membrane mechanic coupling for an axisymmetric geometry using the finite element method (FEM) in COMSOL Multiphysics for Figure 6. A power law fit is used to plot the data of the points from the FEM simulation of an electrostatic membrane. The continuum membrane model differs from the sdof model in the shape of the pull-in curve, but gives rise to a number of additional modes which may all become unstable if the real part of the eigenvalue or pole associated with each mode has a positive real part. Due to the shape of the membrane pull-in curve (as described in Section IV.A), our results were limited by dielectric breakdown of the air. If a deeper depth were possible as would be the case for certain altitudes in space where the dielectric breakdown voltage is favorably large, then stabilization of the additional modes using a multi-input multi-output (MIMO) controller would be necessary. For instance, Lang and Staelin [12] explores the stabilization of higher order modes.

Linearizing Equation (14) results in

$$\dot{\mathbf{x}}(t) = \begin{bmatrix} \dot{x}_1(t) \\ \dot{x}_2(t) \\ \dot{x}_3(t) \end{bmatrix} = \underbrace{\begin{bmatrix} 0 & 1 & 0 \\ -1 & -2\zeta & \frac{2}{3}X_3 \\ \frac{1}{\tau}X_3 & 0 & \frac{1}{\tau}(X_1 - 1) \end{bmatrix}}_{A(X_1, X_3)} \begin{bmatrix} x_1 \\ x_2 \\ x_3 \end{bmatrix} + \begin{bmatrix} 0 \\ 0 \\ \frac{2}{3\tau} \end{bmatrix} v. \quad (16)$$

Note that the eigenvalues of A governing the system dynamics become unstable for operating points where X_1 is past the pull-in displacement of 1/3. This system can be further extended to include the effect of beam steering by asymmetric actuation.

The digital control scheme for this system is shown in Figure 7. Although many more sophisticated control implementations are possible for similar electrostatic systems often for MEMS [27], a proportional-integral controller implemented on a myRIO FPGA running at 100 kHz was found sufficient to stabilize the system with simplicity in implementation. We found that the inherent damping in the system was sufficient that no lead compensation was necessary to stabilize past pull-in. In practice, we were limited by the arcing distance since the mesh was at atmospheric

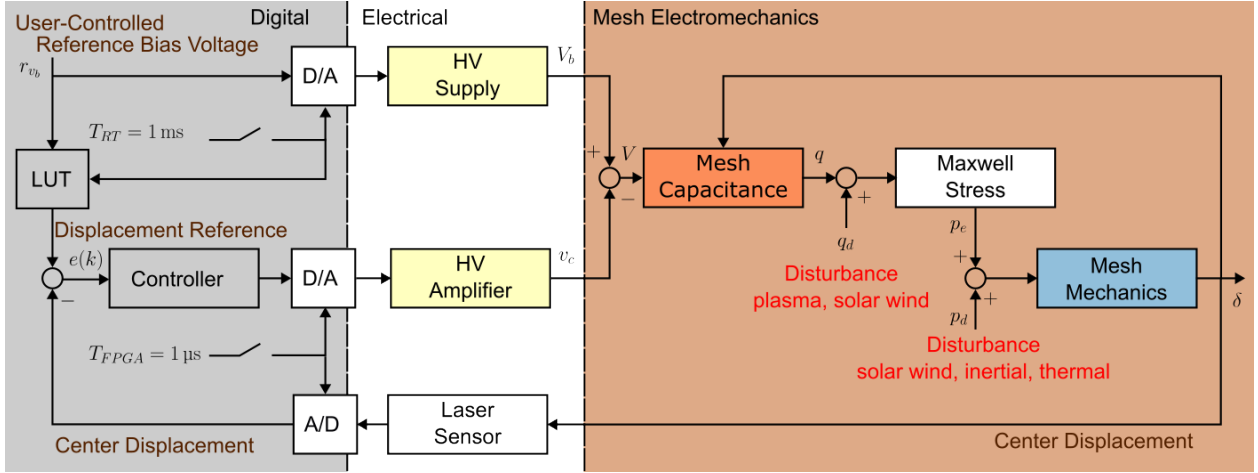


Fig. 7 Block diagram of the control scheme for closed-loop electrostatic actuation.

pressure. If a greater depth were possible, a lead compensator would be necessary to phase stabilize the system at crossover. For the closed loop reference, a look-up table (LUT) was used to interpolate the pull-in curve to decide the proper displacement given an input bias voltage. This was done to prevent the system from controlling the high voltage supply automatically, for which we deemed manual operation to be safer. The LUT was implemented on the myRIO real-time processor (RT) running at 1 kHz. The HV electronics used were a HV supply capable of 30 kV output with slow slew-rate and a fast HV amplifier capable of ± 5 kV with a bandwidth greater than 1 kHz. A Keyence laser displacement sensor with a sampling rate of 1 kHz was used to measure the displacement at a point on the mesh near the center for feedback control. The gains were chosen based on the sdof model and tuned on the real 1-meter prototype.

The block diagram of Figure 7 illustrates how the voltages sum across the mesh and command surface and how the generalized mesh capacitance $Q = \tilde{Q}(V, x)$ gives rise to a charge. This charge is then converted to a force or moment via the Maxwell stress tensor that acts on the mechanical part of the mesh resulting in a displacement x . In this diagram, the nonlinearity arises in the Maxwell stress and electromechanic coupling. It is also possible to include disturbances from sources such as plasma, thermal loads, solar wind, etc.

IV. Results: Reflector Implementation

To assess the performance of our reflector prototype, we measured its radiation patterns at the Compact Range Facility of MIT Lincoln Laboratory, a temperature-controlled RF anechoic chamber [18]. The testing setup in Figure 8 shows the reflector prototype attached to a rotater assembly via an aluminum extrusion support structure. The radiation patterns were measured by rotating this assembly in the azimuth direction (ϕ) and measuring the reflected amplitude and phase of the signal. For our prototype, all radiation patterns were measured at 10 GHz (X-band), with a standard 8.2 GHz to 12.4 GHz feed horn and an angular resolution of 0.5° . During each measurement, the mesh surface was deformed into a curved shape using electrostatic actuation, via the actuation and control schemes presented in Section III.C. The laser displacement sensor and high voltage power electronics which enabled this electrostatic actuation were placed behind the reflector prototype (see Figure 2) and attached to the aluminum extrusion support structure. Below we present the results obtained with 1) open- and closed-loop electrostatic actuation and 2) beam steering.

A. Open- and Closed-Loop Electrostatic Actuation

To function as a reflector, the mesh surface was electrostatically actuated into a curved shape by applying a potential difference across the mesh and command surface with both open-loop and closed-loop controllers. The measured voltage versus displacement data during actuation is plotted in Figure 9, obtained via a laser displacement sensor placed approximately below the center of the mesh. The plot shows a nonlinear increase in displacement with voltage as the mesh approaches the pull-in instability ($v^* \approx 26.2$ kV, $x^* \approx 38$ mm), near which the displacement begins to increase rapidly as the slope approaches infinity. Initially, the controller is turned off in the open-loop stable regime. The controller is only enabled when the displacement crosses the threshold displacement x^* , after which the HV

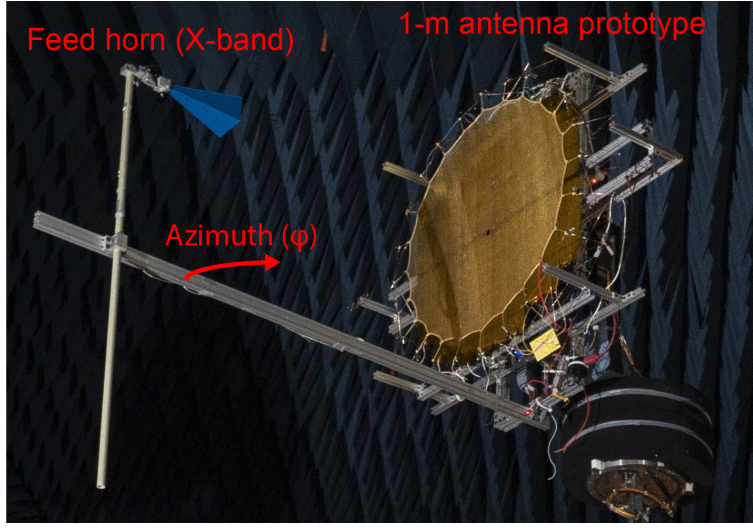


Fig. 8 Image of our prototype at the Compact Range Facility of MIT Lincoln Laboratory. Radiation patterns were measured at 10 GHz with a standard 8.2 GHz to 12.4 GHz feed horn and an azimuth angular resolution of 0.5°.

amplifier adjusts the command surface voltage to stabilize the system at a given reference displacement. The reference displacement past pull-in is computed using an interpolated look-up table (LUT) that computes the desired displacement past pull-in given a manually set voltage (see Section III.C). On this stabilized path, the displacement continues to increase with decreasing voltage difference, as shown by the data points $\delta > x^*$ in Figure 9.

To verify stabilization past pull-in, we turned off the closed-loop controller at the maximum mesh displacement of $\delta_{CL} = 42.35$ mm (red point) and reramped to the same bias voltage with the open loop controller. With the open loop controller we observed the lower mesh displacement of $\delta_{OL} = 26$ mm (blue point), suggesting that the closed loop controller had indeed stabilized the system past the pull-in point of $x^* \approx 38$ mm.

Comparing the pull-in curve of Figure 9 with the analytical sdof model of Section III.C, we see it follows a similar curve with distinct sections before and after the pull-in point. However the measured location of the pull-in point is greater than the $x^* = d/3 \approx 23.3$ mm predicted by the sdof model. This discrepancy can be attributed to the increased geometrical and constitutive nonlinearity of the mesh as it deforms to a curved shape, which is not captured by the linear spring of the sdof model. In comparison, a membrane model pull-in curve predicts a pull-in point of $x^* \approx 0.43d \approx 30$ mm much closer to the observed value.

To characterize the deformation of the mesh during electrostatic actuation, we used Digital Image Correlation (DIC) to measure the mesh surface at the four labeled points of Figure 9. We used two 5 megapixel CMOS cameras (Imager M-lite) to collect images and filtered and processed the data with the LaVision StrainMaster software [28]. The results, plotted in Figure 10 as contour plots, show roughly parabolic surfaces and increasing mesh displacement with greater electrostatic actuation. The nadir point of the mesh surface varies slightly with increasing displacement, suggesting some asymmetry during the deformation. Also the laser displacement sensor is not perfectly aligned with the nadir point, so the measured mesh displacements of Figure 9 do not perfectly correspond with the maximum displacements.

To characterize the performance of the reflector under open- and closed-loop actuation, we measured its radiation patterns in the azimuth range $\varphi \in [-30^\circ, 30^\circ]$, at the Compact Range Facility of MIT Lincoln Laboratory. Given the mesh diameter of $D \approx 0.95$ m, the feed horn was placed at a focal distance of $f = 1.31$ m to achieve peak gain when the mesh was displaced to $\delta = 42.4$ mm, corresponding to a focal length-to-diameter ratio of $f/D = \frac{D}{16\delta} \approx 1.4$. The measured radiation patterns with this setup are plotted in Figure 11 along with a table of measured maximum gain and half-power beamwidth values. While the angular resolution of the measurements was 0.5°, a 1D spline interpolation was used to extract maximum gain and beamwidth values from the measured data. With no actuation, i.e. a flat mesh, we measured a relatively low maximum gain and a defocused beam. However as we increased the bias voltage and actuated the mesh into a curved surface, the maximum gain increased and the beam became more focused, as evidenced by the gain and beamwidth measurements of Figure 11. At the maximum mesh deflection of $\delta_{max} = 42.35$ mm with closed-loop actuation, we obtained the sharpest peak with a maximum gain of $G = 33.4$ dBi and a half-power beamwidth

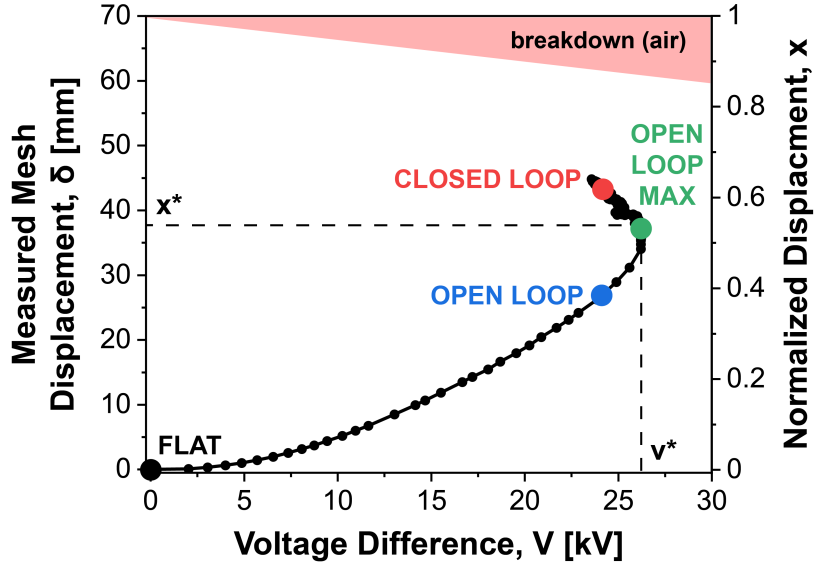


Fig. 9 Measured voltage across the mesh and command surface (V) vs. displacement (x) curve. The pull-in instability occurs near the bias voltage $v^* \approx 26.2$ kV and mesh displacement $x^* \approx 38$ mm, when the displacement increases rapidly with voltage. With closed-loop actuation, we demonstrate stabilization of this instability and displacements above $\delta > x^*$. Compared to the ideal breakdown of air for the electric field strength between parallel plates, arcing occurs much earlier at 45 mm due to the field concentration at sharp corners.

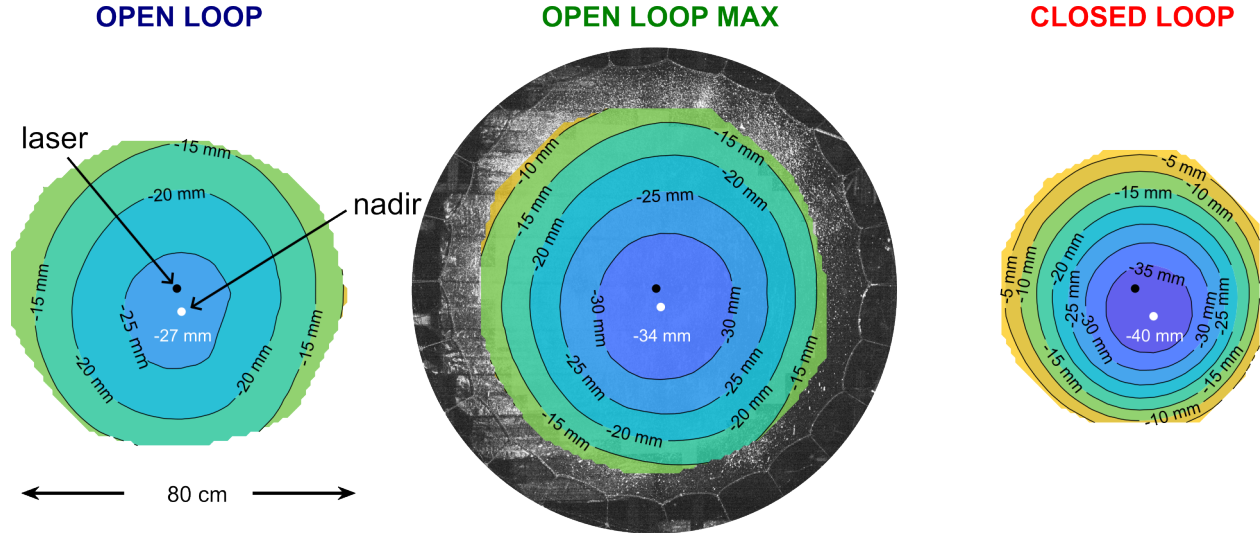


Fig. 10 DIC measurements of the mesh surface under open- and closed-loop electrostatic actuation. The three surfaces show the out-of-plane mesh deflection corresponding to the labeled points in Figure 9 and radiation patterns in Figure 11.

of HPBW = 2.8°. For comparison, analytical estimates of gain and half-power beamwidth for a parabolic reflector at X-band, assuming an approximate efficiency of $\eta \approx 60\%$, are [29]:

$$G^* = 10\log_{10}(\eta(\frac{\pi D}{\lambda})^2) \approx 37.7 \text{ dBi}, \quad (17)$$

$$\text{HPBW}^* = \frac{70\lambda}{D} \approx 2.2^\circ. \quad (18)$$

The analytical estimates are reasonably close to the experimental results, given various potential sources for a

reduced aperture efficiency. For example, reflections from the Bend-Formed structure and mounting components produced unpredictable interference. Additionally, all manufacturing and assembly of the reflector prototype was completed by hand, resulting in mm/cm-scale errors which affect performance given the ~ 3 cm wavelength. The antenna feed was also a common pyramidal horn not optimized for the reflector, resulting in excess spillover as indicated by the higher side lobes in the radiation patterns of Figure 11.

	Measured Mesh Displacement [mm]	Maximum Gain [dBi]	Half-power Beamwidth [$^{\circ}$]
FLAT	0	22.1	9.8
OPEN LOOP	26	29.2	7.4
OPEN LOOP MAX	37	33.2	3.9
CLOSED LOOP	42.35	33.4	2.8

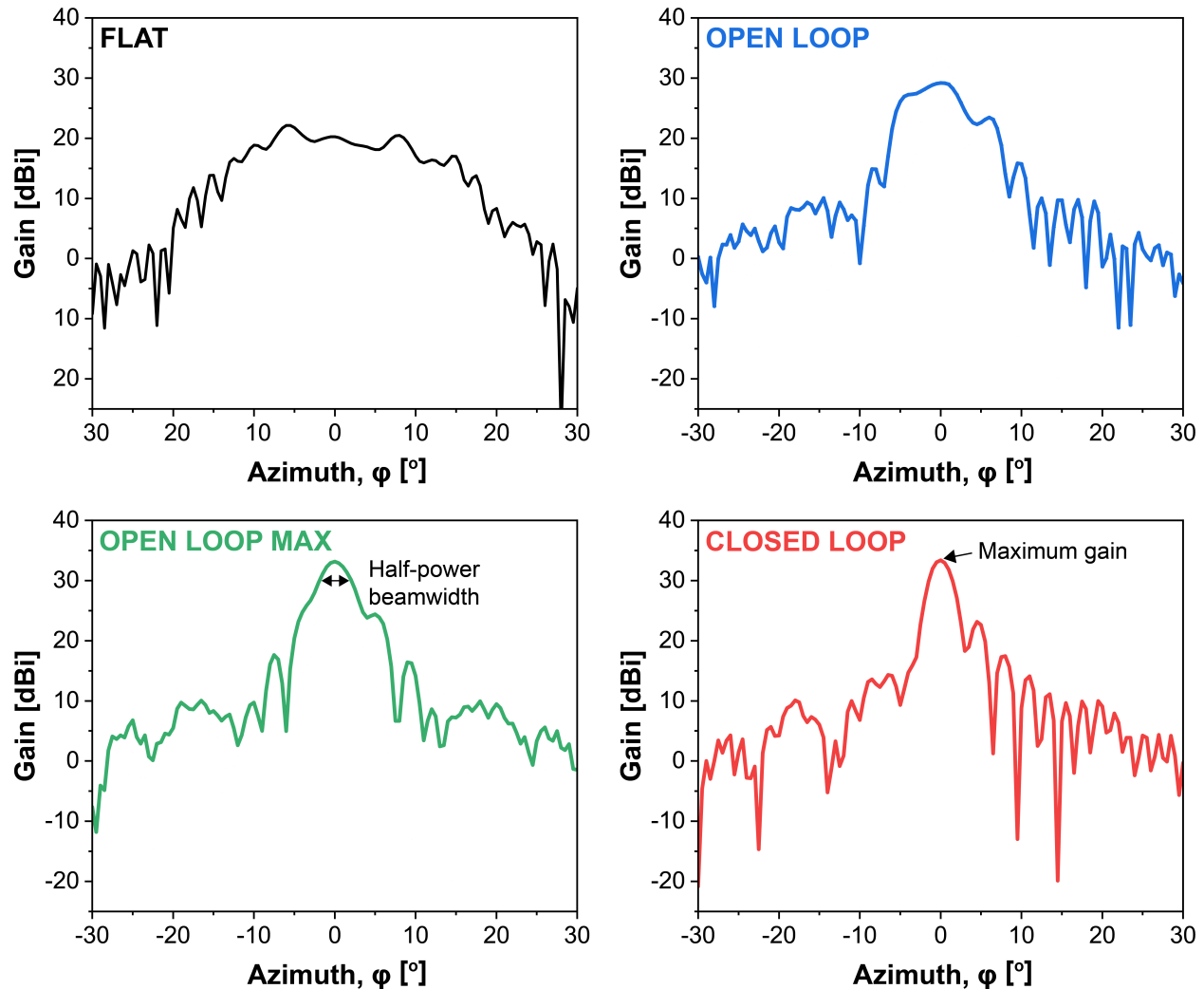


Fig. 11 Measured radiation patterns under open- and closed-loop electrostatic actuation, corresponding to the four labeled points in Figure 9. We demonstrate focusing of the beam with electrostatic actuation and measure the sharpest peak (in red) with gain $G = 33.4$ dBi and half-power beamwidth HPBW = 2.8° .

The results of Figure 11 demonstrate the electrostatically-actuated reflector prototype performs similarly to a parabolic

reflector. Additionally the decreasing beamwidth with increasing mesh displacement demonstrates that electrostatic actuation actively focuses the beam. Unlike a perfect parabolic reflector, the radiation patterns of Figure 11 show asymmetry about the zero azimuth angle. This asymmetry may be attributed to variations in the gap distance across the reflector diameter, which result in asymmetric electrostatic forces and hence asymmetry in the mesh surface (as evidenced by the contour plots of Figure 10). The presence of an additional side lobe at $\varphi \approx 5^\circ$ also suggests some interference during the measurements, possibly from the Bend-Formed support structure around the mesh or the aluminum extrusion support structure on the testing stand.

B. Beam Steering

The reflector prototype was also used to demonstrate beam steering with electrostatic actuation. For large reflectors, this capability can eliminate the need to mechanically slew the entire spacecraft, which becomes difficult due to the lower damping and natural frequencies of the support structures. With electrostatic actuation, we can achieve the same beam steering by asymmetrically deforming the mesh surface. To demonstrate this capability on our prototype, we connected the high voltage amplifier to one half of the command surface with the other side grounded; and varied the amplifier control voltage between $v_c \in [-5 \text{ kV}, 5 \text{ kV}]$ to adjust the electrostatic force on one side of the mesh. Again we used DIC to measure the mesh surface under this asymmetric actuation. The results, plotted in Figure 12 as contour plots, show a rightward shift of the nadir of up to 5 cm as the amplifier voltage is increased from $v_c = +1 \text{ kV}$ to $+5 \text{ kV}$. Implementing this asymmetric actuation in both directions, we measured the radiation patterns plotted in Figure 13, all at the maximum open loop displacement of $x = 37 \text{ mm}$ and for the azimuth range $\varphi \in [-15^\circ, 15^\circ]$. We found varying the amplifier control voltage shifted the azimuth angle of the main lobe, thereby demonstrating beam steering. The relationship between amplifier control voltage and beam steering angle, also plotted in Figure 13, appeared roughly linear with a slope of 0.42 but asymmetric about the zero azimuth angle, possibly due to asymmetries in the mesh deformation. Nonetheless, for the given range of amplifier voltage, we observed a maximum beam steering angle of $\Delta\varphi = 4.2^\circ$. Interestingly the amplifier voltage also caused variations in the maximum gain within $\Delta G = 1.2 \text{ dBi}$, suggesting further focusing of the beam with asymmetric actuation and a slightly rotated feed horn biased towards the negative beam steering angle.

Using electrostatic actuation and an appropriate command surface electrode pattern, it is possible to use beam steering to point the reflector. In the future, with a MIMO control scheme and a more sophisticated electrode pattern, it is possible to use asymmetric actuation for other applications such as shape correction or aperture shaping [3].

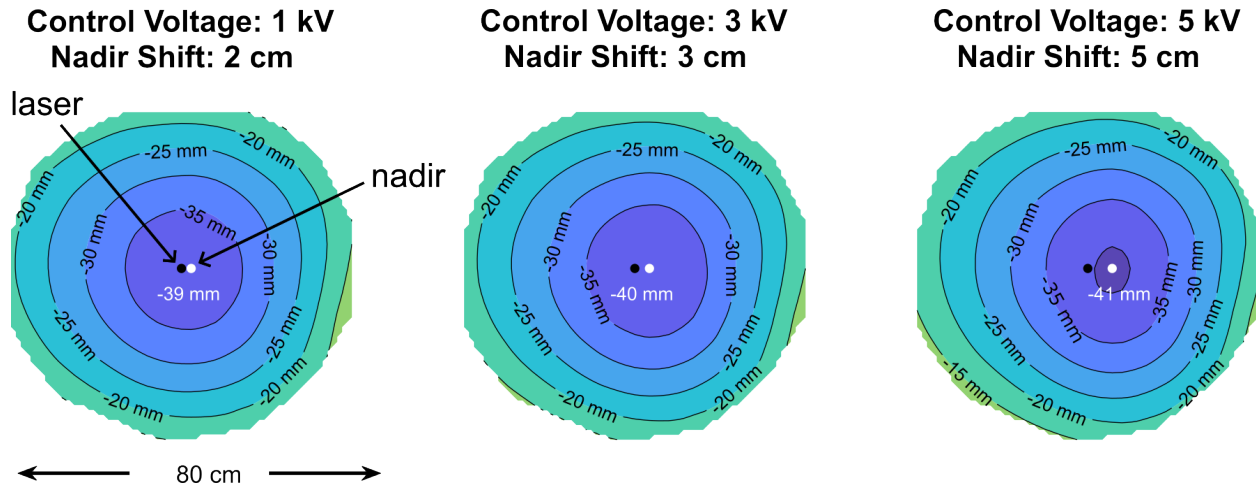


Fig. 12 DIC measurements of the mesh surface during beam steering. The three surfaces show the out-of-plane mesh deflection corresponding to the radiation patterns in Figure 13 with a positive amplifier voltage. Each contour is labeled with the amplifier voltage and the resulting nadir shift.

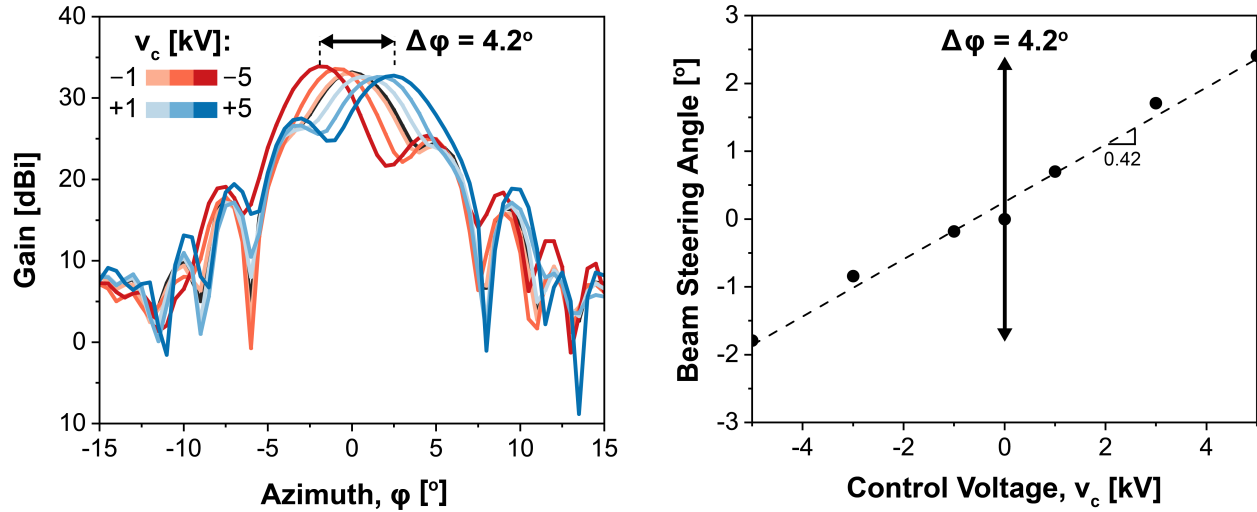


Fig. 13 Measured radiation patterns during beam steering and the relationship between amplifier control voltage and beam steering angle. The patterns demonstrate beam steering of up to $\Delta\phi = 4.2^\circ$ with a control voltage between $v_c \in [-5 \text{ kV}, 5 \text{ kV}]$.

V. Outlook

This paper presented a demonstration of an electrostatically-actuated mesh reflector, potentially suitable for large reflector antennas in space. Our 1-meter diameter prototype consisted of three main structural components: a 40 OPI gold-molybdenum mesh as the reflector surface; a wireframe support structure fabricated with Bend-Forming; and individually addressable CFRP electrodes. This prototype was used to demonstrate open-loop, closed-loop, and asymmetric electrostatic actuation of the metallic mesh surface, using a 30-kV power supply, a ± 5 -kV high-bandwidth amplifier, a myRIO embedded device with real-time processor and FPGA, and a laser displacement sensor. The performance of the electrostatically-actuated mesh surface as a reflector was measured with radiation patterns in an RF anechoic chamber. The radiation patterns showed similar performance to a parabolic reflector, with errors resulting from asymmetries in the deformation and interference from the supporting structures. The radiation patterns also demonstrated active focusing of the beam with open- and closed-loop actuation and beam steering of up to 4.2° with asymmetric actuation. These results establish the feasibility of using electrostatic actuation for forming a mesh reflector, e.g., variable f/D and beam steering—not otherwise achievable with conventional means.

To our knowledge this prototype is the first demonstration of closed-loop and asymmetric electrostatic actuation of a metallic mesh surface to form a reflector. As metallic meshes are commonly used for deployable RF antennas in space, this prototype represents a novel architecture for achieving reflector antennas with actively-controlled mesh surfaces, for applications such as *in-situ* correction of surface distortions, adjustable focal length, and beam steering. Additionally, the fabrication process of Bend-Forming and the CFRP electrodes may enable the in-space manufacturing of such antennas for applications which require large apertures and high precision, such as continuous climate monitoring from geostationary orbit.

Future work is needed to understand the potential for fabricating large electrostatically-actuated mesh reflectors on orbit. Some key trade studies are the scaling of the bias voltage, required power, and slew rate with antenna size. Additionally, the effect of the space environment on electrostatic actuation is not well understood. Here we present simple analyses which estimate these effects and motivate future work on the subject.

A. Environmental Effects

The primary source of power draw is the plasma environment in orbit that would act also as a disturbance on the charge. Compared to the latent power draw of the amplifier and control circuitry and the joule heating of the conductors, we expect the effect of environmental plasma to dominate the power draw. A positively or negatively charged plasma would effectively siphon an extra amount of charge from the amplifier that would result in more power draw. As a simple approximation, we neglect effects of the applied voltage and resulting field from the antenna, and we assume the charging is dominated by the more mobile electrons, as their mass is much smaller relative to ions. For the case in which

the reflector surface is oriented in the ram direction, it is actuated with a positive polarity, and ignoring plasma sheath effects, the electron current density may be approximated between $1\text{-}5 \mu\text{A}/\text{m}^2$ for GEO and $1\text{-}10 \text{ mA}/\text{m}^2$ for LEO [30]. Using $P = IV$, for $V = 30 \text{ kV}$ and a 100-m diameter reflector, the resulting power draw is thus on the order of 10^2 W in GEO and $10^5 - 10^6 \text{ W}$ in LEO. Our calculation is similar to that carried out by Janhunen [31]. A useful metric would be to compare the estimates for electric sail power consumption with measured power draw as more flight experiments are conducted. Consequently, the reflector is well suited as a low-power solution for GEO applications. In GEO, however, the plasma sheath composes a larger volume than in LEO and the resulting power requirement would vary [32, 33]. Furthermore, due to the lower ion current densities, a negative polarity on the bias voltage would potentially further reduce the power requirements [32, 33]. Since the ion velocities are significantly slower than the electron velocities, the mesh would only collect ions by “plowing” into them on orbit. We expect these power estimates to be upper bounds since in realizable reflector at 100 meters, we would take advantage of the voltage scaling discussed in Section V.B to reduce the voltage requirements and thus the power by an order of magnitude.

Another source of potential disturbance is the charge and pressure due to solar wind. For a sufficiently large reflector diameter, the stresses normally beneficial in e-sails [31, 34] might result in a detrimental disturbance on the mesh. One method of mitigation would be to use a bias voltage with negative polarity so as to prevent repulsion of ions.

Many references [35] have been published on the topic of spacecraft charging and the power draw would ultimately depend on the size of the reflector and the orbit conditions. Furthermore, the electronics used in this initial study were designed specifically for ground testing. Flight-ready HV hardware would have different requirements on performance [36]. The same plasma will also result in a net charge disturbance on the mesh, which will need to be corrected by the electrostatic control scheme to maintain the desired electrostatic force.

More detailed analyses on the effect of plasma disturbances, drag, and solar wind on electrostatically-actuated reflectors are left to a forthcoming paper.

B. Voltage Requirement Scaling with Reflector Size

By considering the pull-in voltage from the sdof model, we can derive an expression for how the voltage requirement scales with the size of the mesh. The pull-in voltage expression scales as

$$v^* \propto \sqrt{\frac{kd^2}{C_0}}. \quad (19)$$

To determine the effective spring constant k for the mesh consider the membrane equation subject to a constant uniform pressure and constant tension

$$\nabla^2 w(r) = -\frac{P}{T}. \quad (20)$$

The solution takes the form of

$$w(r) = \frac{P}{T} \frac{D^2 - 2r^2}{8}, \quad (21)$$

allowing us to write the effective spring constant as

$$k \equiv \frac{PA}{w(r=0)} = \frac{8TA}{D^2} \propto T, \quad (22)$$

which scales linearly with tension, but crucially does not scale with the diameter. For this analysis, we assume that the mesh tension is kept constant for all diameters as a common tension is needed to pull out wrinkles in the mesh. For a flat command surface, the gap must scale with the diameter in order to accommodate the same f/D . In this case, the final result is that

$$v^* \propto \sqrt{D}. \quad (23)$$

For a curved command surface contoured such that the gap is constant everywhere once the desired f/D is achieved, the scaling relation becomes

$$v^* \propto \frac{1}{\sqrt{D}}. \quad (24)$$

Using these scaling relations, for a 100-meter diameter dish with a flat electrode the required voltage to reach pull-in would be on the order of 260 kV for a flat command surface and 2.6 kV for a curved electrode that maintains a constant gap at the desired f/D . Therefore, the shape of the command surface plays a critical role in scaling up electrostatic actuation to larger reflectors.

C. Slew Rate & RMS Surface Accuracy

For large space structures, especially mesh reflectors, the bottleneck to slew rate is the settling time of the structure and the mesh itself after slewing due to the high quality factor, i.e., low damping of the system. The primary advantage of the electrostatic actuation scheme is that the actuator is collocated with the mesh in contrast with reaction wheels located on the satellite body. This allows the use of closed-loop control to add damping to the system to decrease settling time while maintaining fast rise times during slew operations. Furthermore, on spacecraft with multiple antennas, electrostatic actuation would allow individual reflectors to be pointed in different directions without need for rigid-body slew operations of the spacecraft that might disturb other antennas.

A preliminary estimate for the deformation magnitude can be obtained as (see [37])

$$x_{\text{rms}} \leq \frac{a_{\text{rms}}}{4\pi^2 f_0^2}, \quad (25)$$

where a_{rms} is the acceleration due to say electrostatic forces and f_0 is the frequency of the fundamental mode. While large accelerations are desired for fast slew operations, surface deformation increases as well. However, with electrostatic actuation it is possible to increase f_0 or the frequency of the dominant poles of the closed-loop system to maintain good surface accuracy even at fast slew rates. A future study on the dynamics of the system will explore the advantages of increased slew rate for electrostatically-actuated mesh reflectors.

VI. Acknowledgements

The authors gratefully acknowledge funding from the MIT Lincoln Laboratory Advanced Concepts Committee and Northrop Grumman Corporation. This work was also supported by the NSF through GRFP Grant Number 1745302. Special thanks to Dr. Christopher Churchill and Mr. Brian Tran, both of Northrop Grumman Corporation, for their assistance in designing and fabricating the mesh surface, and to Mr. Andy Kwas, whose vision and unwavering support made this work possible.

References

- [1] Powell, R., "A future for large space antennas," *7th Communications Satellite Systems Conference*, 1978, p. 588.
- [2] Hedgepeth, J. M., "Influence of fabrication tolerances on the surface accuracy of large antenna structures," *Aiaa Journal*, Vol. 20, No. 5, 1982, pp. 680–686.
- [3] Thomson, M., "Astromesh deployable reflectors for ku and ka band commercial satellites," *20th AIAA international communication satellite systems conference and exhibit*, 2002, p. 2032.
- [4] Banik, J., "Realizing large structures in space," *Proc., Frontiers of Engineering: Reports on Leading-Edge Engineering from the 2015 Symp*, 2016, pp. 55–62.
- [5] Taminger, K., and Hafley, R. A., "Electron beam freeform fabrication: a rapid metal deposition process," *3rd annual automotive composites conference*, 2003.
- [6] Kugler, J., Cherston, J., Joyce, E. R., Shestopole, P., and Snyder, M. P., "Applications for the archinaut in space manufacturing and assembly capability," *AIAA SPACE and astronautics forum and exposition*, 2017, p. 5365.
- [7] Levedahl, B., Hoyt, R. P., Silagy, T., Gorges, J., Britton, N., and Slostad, J., "Trusselator™ technology for in-situ fabrication of solar array support structures," *2018 AIAA Spacecraft Structures Conference*, 2018, p. 2203.
- [8] N79-29213, N. R., "Space Fabrication Demonstration System: Final Report, Technical Volume," Tech. rep., Grumman Aerospace Corp., Bethpage, NY, United States, 1979.
- [9] Bhundiya, H. G., "Bend-Forming: A Deformation Process for In-Space Manufacturing of Truss Structures," Master's thesis, Massachusetts Institute of Technology, 2022.
- [10] Bhundiya, H. G., Royer, F., and Cordero, Z., "Engineering Framework for Assessing Materials and Processes for In-Space Manufacturing," *Journal of Materials Engineering and Performance*, 2022, pp. 1–15.
- [11] Lang, J. H., and Staelin, D. H., "Electrostatically-controlled large-aperture reflecting satellite antennas," *1980 19th IEEE Conference on Decision and Control including the Symposium on Adaptive Processes*, IEEE, 1980, pp. 991–993.

- [12] Lang, J., and Staelin, D., "The computer-controlled stabilization of a noisy two-dimensional hyperbolic system," *IEEE Transactions on Automatic Control*, Vol. 27, No. 5, 1982, pp. 1033–1043.
- [13] Mihora, D. J., and Redmond, P. J., "Electrostatically formed antennas," *Journal of Spacecraft and Rockets*, Vol. 17, No. 5, 1980, pp. 465–473.
- [14] Chodimella, S., Moore, J., Otto, J., and Fang, H., "Design evaluation of a large aperture deployable antenna," *47th AIAA/ASME/ASCE/AHS/ASC Structures, Structural Dynamics, and Materials Conference 14th AIAA/ASME/AHS Adaptive Structures Conference 7th*, 2006, p. 1603.
- [15] Gu, Y., Duan, B., and Du, J., "The establishment and application of direct coupled electrostatic-structural field model in electrostatically controlled deployable membrane antenna," *Acta Astronautica*, Vol. 146, 2018, pp. 185–191.
- [16] Duan, B., Zhang, Y., and Du, J., "Electrostatic Forming Membrane Reflector Antenna," *Large Deployable Satellite Antennas*, Springer, 2020, pp. 241–271.
- [17] Mobrem, M., Kuehn, S., Spier, C., and Slimko, E., "Design and performance of astromesh reflector onboard soil moisture active passive spacecraft," *2012 IEEE Aerospace Conference*, IEEE, 2012, pp. 1–10.
- [18] Shields, M. W., and Fenn, A. J., "A new compact range facility for antenna and radar target measurements," Tech. rep., Massachusetts Institute of Technology-Lincoln Laboratory Lexington United States, 2007.
- [19] Zhang, W.-M., Yan, H., Peng, Z.-K., and Meng, G., "Electrostatic pull-in instability in MEMS/NEMS: A review," *Sensors and Actuators A: Physical*, Vol. 214, 2014, pp. 187–218.
- [20] Labs, P., "D.I. Wire Pro Info," <https://aetlabs.com/wp-content/uploads/D.I.WireProinfo.pdf>, 2022. Accessed 30 May 2022.
- [21] Glover, J. D., Overbye, T. J., and Sarma, M. S., *Transmission Line Parameters*, 6th ed., Cengage Learning, 2016.
- [22] Royer, F., and Pellegrino, S., "Ultralight ladder-type coilable space structures," *2018 AIAA Spacecraft Structures Conference*, 2018, p. 1200.
- [23] Schlothauer, A., Royer, F., Pellegrino, S., and Ermanni, P., "Flexible Silicone Molds for the Rapid Manufacturing of Ultra-Thin Fiber Reinforced Structures," *SAMPE Conf. Proc., Long Beach, CA*, 2018.
- [24] Hayden, J., "The dielectric strength of the vacuum: Electrostatic ionization gradient of metal electrodes," *Journal of the American Institute of Electrical Engineers*, Vol. 41, No. 11, 1922, pp. 852–853.
- [25] Wang, P., Gutierrez, R., and Bartman, R., "A method for designing electrostatic-actuator electrode pattern in micromachined deformable mirrors," *Sensors and Actuators A: Physical*, Vol. 55, No. 2-3, 1996, pp. 211–217.
- [26] Chang, P., Chang, C., and Yen, K., "Design of microelectrode arrays for electrostatic microactuators and capacitive microsensors," *Journal of intelligent material systems and structures*, Vol. 9, No. 2, 1998, pp. 95–103.
- [27] Dong, L., and Edwards, J., "Closed-loop voltage control of a parallel-plate MEMS electrostatic actuator," *Proceedings of the 2010 American Control Conference*, IEEE, 2010, pp. 3409–3414.
- [28] LaVision, "2D/3D Stereo DIC - StrainMaster," <https://www.lavision.de/en/products/strainmaster/index.php>, 2022. Accessed 1 December 2022.
- [29] Balanis, C. A., *Antenna theory: analysis and design*, John wiley & sons, 2015.
- [30] Hastings, D., and Garrett, H., *Plasma Interactions*, Cambridge Atmospheric and Space Science Series, Cambridge University Press, 1996, p. 142–207. <https://doi.org/10.1017/CBO9780511525032.006>.
- [31] Janhunen, P., "Electric sail for spacecraft propulsion," *Journal of Propulsion and Power*, Vol. 20, No. 4, 2004, pp. 763–764.
- [32] NASA, "Mitigating In-Space Charging Effects - A Guideline," Tech. rep., NASA, 2022.
- [33] NASA, "Low Earth Orbit Spacecraft Charging Design Handbook," Tech. rep., NASA, 2018.
- [34] Bassetto, M., Niccolai, L., Quarta, A. A., and Mengali, G., "A comprehensive review of Electric Solar Wind Sail concept and its applications," *Progress in Aerospace Sciences*, Vol. 128, 2022, p. 100768.
- [35] Lai, S. T., "Fundamentals of spacecraft charging," *Fundamentals of Spacecraft Charging*, Princeton University Press, 2011.

- [36] Bever, R. S., Ruitberg, A. P., Kellenbenz, C. W., and Irish, S. M., "High voltage power supply design guide for space," Tech. rep., 2006.
- [37] Lake, M. S., Peterson, L. D., and Levine, M. B., "Rationale for defining structural requirements for large space telescopes," *Journal of spacecraft and rockets*, Vol. 39, No. 5, 2002, pp. 674–681.